Effects of Cs$_2$CO$_3$ Additive in KOH Electrolyte Used in Ni/MH Batteries

Shuli Yan [1,2], Jean Nei [2] [iD], Peifeng Li [1,2], Kwo-Hsiung Young [1,2,*] [iD] and K. Y. Simon Ng [1]

[1]   Department of Chemical Engineering and Materials Science, Wayne State University, Detroit, MI 48202, USA; shuli.yan@partners.basf.com (S.Y.); peifeng.li@partners.basf.com (P.L.); sng@wayne.edu (K.Y.S.N.)

[2]   BASF/Battery Materials—Ovonic, 2983 Waterview Drive, Rochester Hills, MI 48309, USA; jean.nei@basf.com

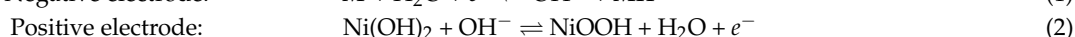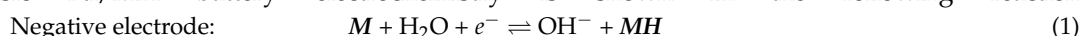*   Correspondence: kwo.young@basf.com; Tel.: +1-248-293-7000

Abstract: The effects of Cs$_2$CO$_3$ addition in a KOH-based electrolyte were investigated for applications in nickel/metal hydride batteries. Both MgNi-based and Laves phase-related body-centered cubic solid solution metal hydride alloys were tested as the anode active materials, and sintered β-Ni(OH)$_2$ was used as the cathode active material. Certain amounts of Cs$_2$CO$_3$ additive in the KOH-based electrolyte improved the electrochemical performances compared with a conventional pure KOH electrolyte. For example, with Laves phase-related body-centered cubic alloys, the addition of Cs$_2$CO$_3$ to the electrolyte improved cycle stability (for all three alloys) and discharge capacity (for the Al-containing alloys); moreover, in the 0.33 M Cs$_2$CO$_3$ + 6.44 M KOH electrolyte, the discharge capacity of Mg$_{52}$Ni$_{39}$Co$_3$Mn$_6$ increased to 132%, degradation decreased to 87%, and high-rate dischargeability stayed the same compared with the conventional 6.77 M KOH electrolyte. The effects of Cs$_2$CO$_3$ on the physical and chemical properties of Mg$_{52}$Ni$_{39}$Co$_3$Mn$_6$ were characterized by Fourier transform infrared spectroscopy, X-ray diffraction, transmission electron microscopy, inductively coupled plasma, and electrochemical impedance spectroscopy. The results from these analyses concluded that Cs$_2$CO$_3$ addition changed both the alloy surface and bulk composition. A fluffy layer containing carbon was found covering the metal particle surface after cycling in the Cs$_2$CO$_3$-containing electrolyte, and was considered to be the main cause of the reduction in capacity degradation during cycling. Also, the Cs$_2$CO$_3$ additive promoted the formations of the C–O and C=O bonds on the alloy surface. The C–O and C=O bonds were believed to be active sites for proton transfer during the electrochemical process, with the C–O bond being the more effective of the two. Both bonds contributed to a higher surface catalytic ability. The addition of 0.33 M Cs$_2$CO$_3$ was deemed optimal in this study.

Keywords: nickel metal hydride battery; electrochemistry; hydrogen storage alloys; nickel hydroxide; alkaline electrolyte; salt additive

1. Introduction

Since the commercialization of nickel/metal hydride (Ni/MH) batteries in 1980s, they have been widely used as energy storage devices in hybrid electric vehicles, vacuum cleaners, electric toys, power tools, and cordless phones, to name a few uses [1–3]. Ni/MH batteries have many superior properties over rival battery technologies, such as high specific power, long cycle life, robust abuse tolerance, and a wide temperature operation range [2]. In the past decades, Ni/MH batteries have repeatedly attracted attention from both researchers and markets.

Basic Ni/MH battery electrochemistry is shown in the following reactions:

Negative electrode: $M + H_2O + e^- \rightleftharpoons OH^- + MH$ (1)

Positive electrode: $Ni(OH)_2 + OH^- \rightleftharpoons NiOOH + H_2O + e^-$ (2)

The reaction taking place at the negative electrode (anode) is described in Equation (1). *M* is a metal hydride (MH) alloy capable of storing hydrogen reversibly, and ***MH*** is the corresponding hydrided metal. During charge, the added voltage splits the water molecule into a proton and a hydroxide ion. Driven by voltage and diffusion difference, protons transfer from the electrolyte to the surface of the MH alloy particles, and then into the bulk of alloy. During discharge, protons travel in a reverse route. Equation (2) represents the reaction at the positive electrode (cathode). During charge, protons are dissociated from $Ni(OH)_2$, then move to the cathode surface, and finally recombine with the hydroxide ions in the electrolyte.

In order to promote proton transfer and improve electrochemical performance, many researchers and companies have focused on developing new anode/cathode materials, with a particular focus on anode materials. A wide set of hydrogen storage MH alloys have been studied for electrochemical applications, including AB_2, AB_5, A_2B_7, body-centered cubic (BCC) solid solution, $BCC-AB_2$ composite, Mg_xNi_y, TiNi and its composite, etc. [4–9]. Yu et al. reported a $Ti_{40}V_{30}Cr_{15}Mn_{15}$ alloy with an initial capacity of 814 mAh·g^{-1} at a rate of 10 mA·g^{-1} and 80 °C, which is more than twofold higher than the capacity obtained from the conventional rare earth-based AB_5 MH alloy (350 mAh·g^{-1}) [10]. However, degradation for this alloy was very high due to the pulverization caused by hydrogen evolution inside MH alloy particles. Young and Nei reported various MgNi-based amorphous/microcrystalline MH alloys with a theoretical capacity as high as 1080 mAh·g^{-1} [11]. However, most of these alloys demonstrated rapid decay during cycling. Nei reported an 80% or higher decay in capacity after 20 cycles for MgNi-based MH alloys [12]. Many methods have been attempted to improve the electrochemical performance of MH alloys. Recently, additives such as B [13], Ti [14,15], Pt [15], Pd [14], Nd [16], Cr [17], La [18], Co [19], Ni [20], Li [21], and Cu [22] were added to the bulk or surface of MH alloys to enhance the capacity, cycle stability, and high-rate dischargeability (HRD). For MgNi-based MH alloys, Ni coating [23], the addition of TiO_2 [24], and substitutions of Mn [25,26] and Nb [26] have been intensively studied with the goal of improving electrochemical performances. Many studies on the alkaline electrolytes [27–49] and salt additives [50,51] were conducted before in NiMH and other alkaline batteries; however, focuses were on the rare earth-based AB_5 and Zr-based AB_2 MH alloys. Young et al. have pointed out that electrolyte modification is one of the most economic and effective methods to alter electrode performances, since it does not affect the battery gravimetric and volumetric energy densities [11]. Nei et al. reported the conductivity and corrosion behaviors of several hydroxides [16]. Later, Yan et al. published a screen test of 32 salt additives in the KOH electrolyte, of which 12 salt additives were found to efficiently decrease the corrosion of the traditional KOH electrolyte on alloy AR3 (an MgNi-based MH alloy with a nominal composition of $Mg_{52}Ni_{39}Co_3Mn_6$) [52]. However, no detailed investigation was done on these 12 salt additives.

This study is a continuous work from Yan's previous report [52]. A systematic investigation of the effects of Cs_2CO_3 addition in a conventional KOH electrolyte on various MH alloys is performed. This additive was originally used in the KOH electrolyte for Ni/Zn batteries to extend the cycle life [53]. The total concentration of Cs_2CO_3 and KOH is fixed at 6.77 M. The influence of Cs_2CO_3 on the cell performance, electrolyte properties, and surface and bulk structure of MH alloy electrodes are examined. A possible proton transfer process for the Cs_2CO_3-containing electrolyte system is also discussed.

2. Experimental Setup

Both the sintered β-$Ni(OH)_2$ and MH alloys (AR3, P31, P32, and P37) were produced in-house. The compositions and fabrication methods of the MH alloys are summarized in Table 1. AR3 is an amorphous/microcrystalline MgNi-based MH alloy made by a melt–spin method, followed by mechanical alloying [52]. The P-series MH alloys belong to a family of Laves phase-related body-centered cubic (BCC) solid solution alloys [54], which were developed during a United States (U.S.) Department of Energy-funded research program [4]. The P-series of alloys were produced by

induction melting, followed by annealing under optimized conditions (900 °C for 12 h [55]). KOH and Cs_2CO_3 were purchased from the Sigma-Aldrich Corporation (St. Louis, MO, USA).

Table 1. Compositions of the four metal hydride (MH) alloys used in this study. BCC: body-centered cubic.

Alloy	Alloy System	Composition	Preparation Method
AR3	Amorphous/microcrystalline MgNi	$Mg_{52}Ni_{39}Co_3Mn_6$	Melt-spin and mechanical alloying
P31	Laves phase-related BCC	$Ti_{15.6}Hf_{2.1}V_{44}Cr_{11.2}Mn_{6.9}Co_{1.4}Ni_{18.5}Al_{0.3}$	Induction melting and thermal annealing
P32	Laves phase-related BCC	$Ti_{15.6}Hf_{2.4}V_{44}Cr_{11.2}Mn_{6.9}Co_{1.4}Ni_{18.5}$	Induction melting and thermal annealing
P37	Laves phase-related BCC	$Ti_{14.5}Zr_{1.7}V_{46.6}Cr_{11.9}Mn_{6.5}Co_{1.5}Ni_{16.9}Al_{0.4}$	Induction melting and thermal annealing

Electrochemical charge/discharge cycling tests were performed with an Arbin BT2000 battery tester (Arbin, College Station, TX, USA) at room temperature. In the test cells, the cathode was sintered β-$Ni(OH)_2$, the anode was made from directly dry-compacting the alloy powder onto an expanded Ni substrate without using any binder, and the separator was hydrophilic nonwoven polyolefin. Charge/discharge processes were the same as reported before by Yan et al. [52] The cell was charged at $100\ mA \cdot g^{-1}$ for 5 h, and discharged first at $100\ mA \cdot g^{-1}$ to a cutoff voltage of 0.9 V. The initial discharge was followed by a 30 s rest for the voltage to recover, and then the cell was discharged at $24\ mA \cdot g^{-1}$ to reach a cutoff voltage of 0.9 V. The cell was put to rest for 30 s again before the final discharge at $8\ mA \cdot g^{-1}$ to 0.9 V. Testing for each alloy/electrolyte combination was repeated three times. When the total discharge capacity (sum of capacities at 100, 24, and $8\ mA \cdot g^{-1}$) of the cell decreased by 70%, it was considered to be cell failure.

Discharge capacity degradation and HRD were calculated and compared with those of a traditional 6.77 M KOH electrolyte. Degradation was determined as Yan previously reported [52]. The percent capacity loss per cycle within the initial 10 cycles is shown by the following equation:

$$\text{Degradation \%} = \frac{Cap_{\text{high}} - Cap_{\text{low}}}{\left(n_{\text{high}} - n_{\text{low}}\right) \times Cap_{\text{high}}} \times 100\% \tag{3}$$

where Cap_{high} is the highest value of discharge capacity achieved in the initial 10 cycles, Cap_{low} is the lowest value of discharge capacity in the initial 10 cycles, n_{high} is the cycle number of the highest discharge capacity in the initial 10 cycles, and n_{low} is the cycle number of the lowest discharge capacity in the initial 10 cycles. HRD is defined as the ratio of capacities measured at 100 and $8\ mA \cdot g^{-1}$.

Fourier transform infrared (FTIR) spectroscopy was performed on a Perkin Elmer Spectrum Spotlight 200™ (Perkin Elmer, Waltham, MA, USA). Powder X-ray diffraction (XRD) patterns were taken with a Rigaku RU2000 rotating anode powder diffractometer (Rigaku Americas Corporation, The Woodlands, TX, USA) equipped with Cu–K_α radiation (40 kV, 200 mA). Transmission electron microscopy (TEM) was carried out using a JEOL 2010 (JEOL, Tokyo, Japan) operated at 200 kV for microstructural and morphological studies. Inductively coupled plasma-optical emission spectroscopy (ICP-OES) was performed on a Perkin Elmer Optima TM 2100 DV ICP-OES system (Perkin Elmer, Waltham, MA, USA). Electrochemical impedance spectroscopy was measured on a Solartron S1287 potentiostat/galvanostat with a S1255 frequency response analyzer (Solartron, Hampshire, UK).
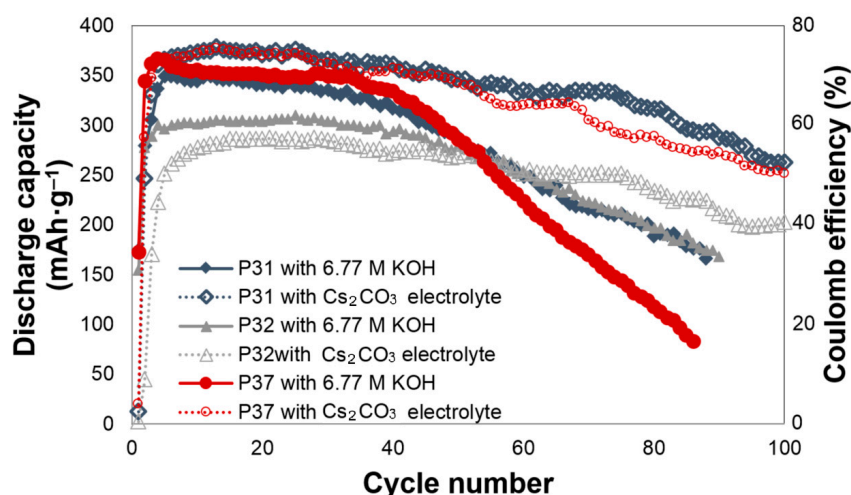
3. Results and Discussion

3.1. Electrochemical Performances for Electrolytes with Cs_2CO_3 Addition

Generally, KOH solutions with concentrations varying from 4.0 M to 8.5 M are used for Ni/MH batteries in the research field and for commercial applications [11,56–58]. In this study, the electrolyte concentration (KOH + Cs_2CO_3) is fixed at 6.77 M. Concentrations of KOH and Cs_2CO_3 in various electrolytes are shown in Table 2.

Table 2. Normalized discharge capacities, degradations, and high-rate dischargeabilities (HRDs) of AR3 cycled in five different electrolytes.

Electrolyte Composition	Normalized Capacity (%)	Normalized Degradation (%)	Normalized HRD (%)
6.77 M KOH	100.00	100.00	100.00
6.44 M KOH + 0.33 M Cs_2CO_3	132.45	86.65	99.86
6.11 M KOH + 0.66 M Cs_2CO_3	120.24	98.30	101.32
5.77 M KOH + 1.00 M Cs_2CO_3	117.62	97.70	91.41
5.44 M KOH + 1.33 M Cs_2CO_3	97.28	87.41	65.25

The effects of Cs_2CO_3 addition on the electrochemical performances of alloys P31, P32, and P37 are shown in Figure 1. All of the cells require approximately three to five cycles to be activated. For alloy P31, Cs_2CO_3 slightly increases the initial discharge capacity, and greatly decreases the degradation. The initial discharge capacities of alloy P31 in the 6.77 M KOH and 6.44 M KOH + 0.33 M Cs_2CO_3 electrolytes are 349 and 375 mAh·g^{-1}, respectively. In the 6.77 M KOH electrolyte, the capacity of alloy P31 begins to fade after the 20th cycle, while the capacity fade begins at the 55th cycle in the 6.44 M KOH + 0.33 M Cs_2CO_3 electrolyte. The same trend was observed in alloy P37, where the addition of Cs_2CO_3 increases the initial discharge capacity from 364 mAh·g^{-1} to 375 mAh·g^{-1}, and changes the beginning of the capacity fade from the 30th to the 65th cycle. For alloy P32, Cs_2CO_3 does not increase the initial discharge capacity; however, it greatly decreases the decay, as shown in Figure 1. In comparison to alloy P32, both alloys P31 and P37 contain Al, raising the possibility that the presence of Al results in the alloy surface reacting with the CO_3^{2-} ions in the electrolyte and forming $Al_2(CO_3)_3$. $Al_2(CO_3)_3$, which is known to be unstable in water [59]. Such phenomenon may assist in the dissolution of Al into the highly alkaline electrolyte, and therefore increase the reactive surface area.

Figure 1. Discharge capacities of alloys P31, P32, and P37 in the 6.77 M KOH and 6.44 M KOH + 0.33 M Cs_2CO_3 electrolytes.

The effects of Cs_2CO_3 on the AR3 alloy electrode performances are shown in Figure 2. The AR3 MH alloy is very reactive to the KOH electrolyte due to the alloy's high content of Mg and the high porosity caused by the mechanical alloying preparation [12]. A rapid decay in the KOH electrolyte was previously reported [5,6,12]. Figure 2 shows an increase in initial discharge capacity and a decrease in capacity decay with the addition of Cs_2CO_3. The discharge capacity, degradation, and HRD of the Cs_2CO_3-containing electrolytes are normalized to those of the 6.77 M KOH electrolyte and presented in Table 2. The optimized conditions were obtained at the concentration of 6.44 M KOH + 0.33 M Cs_2CO_3, which exhibited the highest discharge capacity and lowest degradation. Table 2 also indicates that a

small addition of Cs_2CO_3 has an insignificant effect on HRD, while a high concentration of Cs_2CO_3 in the electrolyte has a negative influence on HRD.
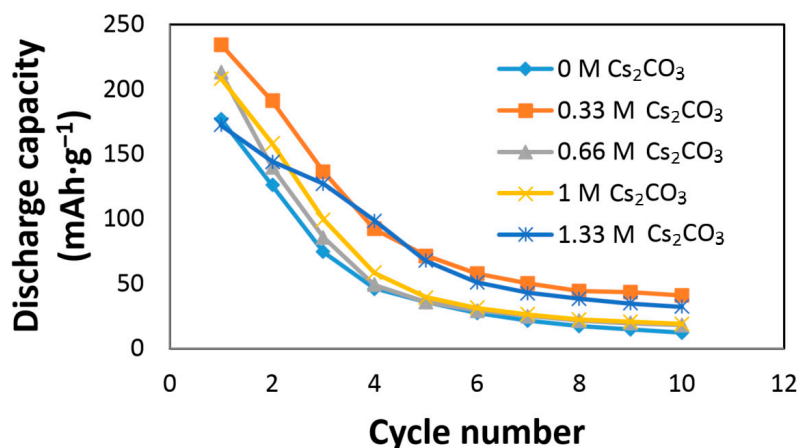

Figure 2. Discharge capacities of AR3 in 6.77 M KOH, 6.44 M KOH + 0.33 M Cs_2CO_3, 6.11 M KOH + 0.66 M Cs_2CO_3, 5.77 M KOH + 1.00 M Cs_2CO_3, and 5.44 M KOH + 1.33 M Cs_2CO_3 electrolytes.

3.2. Effects of Cs_2CO_3 Addition on MgNi Alloy

Weights of the cycled AR3 alloy electrodes were measured. After 10 cycles, weights of the alloy electrodes cycled in all of the electrolytes increased due to surface metal oxidation and the deposition of some salts. Surface metal oxidation during charge leads to the formation of surface metal hydroxide, such as $Mg(OH)_2$ [11,16]. The majority of salt depositions are carbonates and bicarbonates [52]. Weight gains of the alloy electrodes cycled in the Cs_2CO_3-containing electrolytes are normalized to that in the 6.77 M KOH electrolyte and presented in Table 3. As the Cs_2CO_3 concentration in the electrolyte increases, the weight gain decreases. The addition of Cs_2CO_3 changes the physical and chemical properties of the electrolyte. Cs_2CO_3 reacts with the MH alloy surface during electrochemical cycling, which results in a protective layer and greatly decreases the reaction rate of metal oxidation. Therefore, the weight gain due to surface oxidation (listed in Table 3) is substantially reduced by the addition of Cs_2CO_3 in the electrolyte.

Table 3. Normalized weight gains of the AR3 alloy electrodes cycled in five different electrolytes.

Electrolyte Composition	Normalized Electrode Weight Gain (%)
6.77 M KOH	100.0
6.44 M KOH + 0.33 M Cs_2CO_3	76.0
6.11 M KOH + 0.66 M Cs_2CO_3	64.8
5.77 M KOH + 1.00 M Cs_2CO_3	54.2
5.44 M KOH + 1.33 M Cs_2CO_3	46.9

TEM micrographs of the cycled AR3 indicate that a thin layer of fluffy material covers the surface of the MH alloy (Figure 3a,b). FTIR was used to characterize the surface structure, and the results are shown in Figure 4. For the fresh MH alloy, there is no clear diffraction peak, which indicates that the alloy surface is clean. For the alloy cycled in the 6.77 M KOH electrolyte, a peak at approximately 1409 cm^{-1} is observed, which is related to the vibration of surface metal–O bonds [60]. For the electrode cycled in the 6.44 M KOH + 0.33 M Cs_2CO_3 electrolyte, the same peak is seen, but shifted slightly to a lower wavelength, implying a decrease in bond strength. However, the peak intensity increases, which suggests the appearance of C–O bonds on the alloy surface, since the stretching vibration of the C–O bond occurs at approximately the same wavelength [61] as the metal–O bond. With further increases in concentration of Cs_2CO_3 in the electrolyte, the metal–O bond becomes weaker with the

peak shifting even lower, to around 1375 cm^{-1}, and the amount of C–O bond decreases, as shown by a reduction in peak intensity compared with the electrode cycled in the 6.77 M KOH electrolyte. Moreover, peaks at approximately 1730 and 1210 cm^{-1} start to appear as the content of Cs_2CO_3 increases, which is related to the vibration of the C=O bond in carbonate [61]. FTIR results demonstrate the changes in the surface groups on the MH alloy surface with varying Cs_2CO_3 concentration.
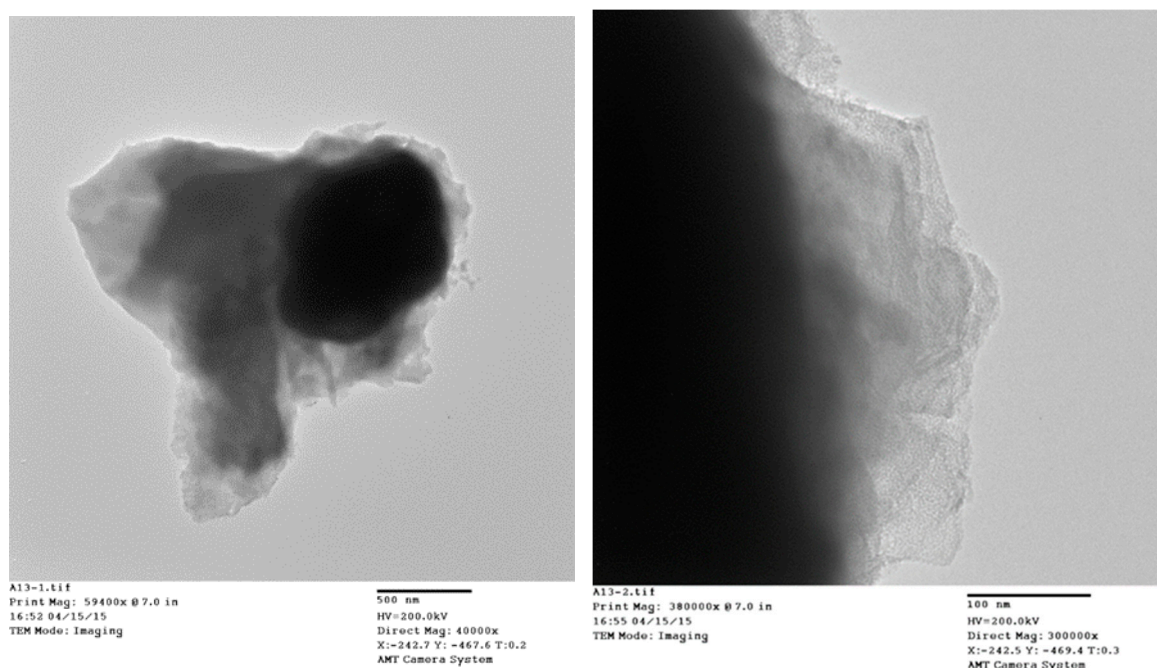

Figure 3. Transmission electron microscopy (TEM) micrographs at (**a**) ×40,400 and (**b**) ×300,000 magnification of AR3 cycled in the 6.44 M KOH + 0.33 M Cs_2CO_3 electrolyte.
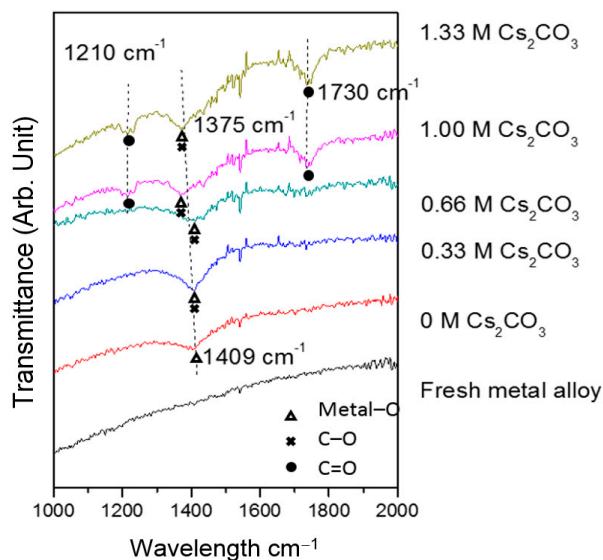

Figure 4. Fourier transform infrared (FTIR) spectra of the fresh and cycled AR3 in the 6.77 M KOH, 6.44 M KOH + 0.33 M Cs_2CO_3, 6.11 M KOH + 0.66 M Cs_2CO_3, 5.77 M KOH + 1.00 M Cs_2CO_3, and 5.44 M KOH + 1.33 M Cs_2CO_3 electrolytes.

XRD patterns before and after electrochemical cycling are shown in Figure 5. As our previous study has shown [62], the two broad peaks at approximately 23° and 42° (marked as "A") are from the

broadening of the $MgNi_2$ and Mg_2Ni phases. These two broad peaks exist in all of the cycled AR3 samples, suggesting high stability for $MgNi_2$ and Mg_2Ni during cycling. Except for the peaks marked as "A", there are some strong peaks related to metallic Mn and Co (marked as "1" and "2" in Figure 5, respectively). Mn and Co fine particles are the remnants from the mechanical alloying process, and act as catalysts for hydrogen storage to enhance the electrochemical capacity [11]. $Mg(OH)_2$ is also found in all of the cycled AR3 (marked as "3" in Figure 5), and is the oxidation product from high-Mg AR3. The peaks at approximately 18° and 33° are the (001) and (100) diffraction peaks for the hexagonal $Mg(OH)_2$. Results from the phase deconvolution by Jade 9.0 software (MDI, Livermore, CA, USA) are summarized in Tables 4 and 5. While no obvious trends are found in the crystallite sizes of phases with cycling in different electrolytes, clear trends are observed in phase abundances. An increase in Cs_2CO_3 concentration in the exchange of KOH reduces both the amount of $Mg(OH)_2$ (decrease in oxidation) and the Mg_2Ni-to-$MgNi_2$ ratio (last column in Table 5). The Mg_2Ni phase is more oxidable compared with the $MgNi_2$ phase, due to its higher Mg content. Upon contacting the KOH electrolyte, the Mg_2Ni phase is oxidized into $Mg(OH)_2$, which results in a reduction in the Mg_2Ni-to-$MgNi_2$ ratio from 1.50 to 0.67. Partial replacement of the corrosive KOH with Cs_2CO_3 increases the Mg_2Ni-to-$MgNi_2$ ratio, which is another indication of decrease in alloy oxidation.
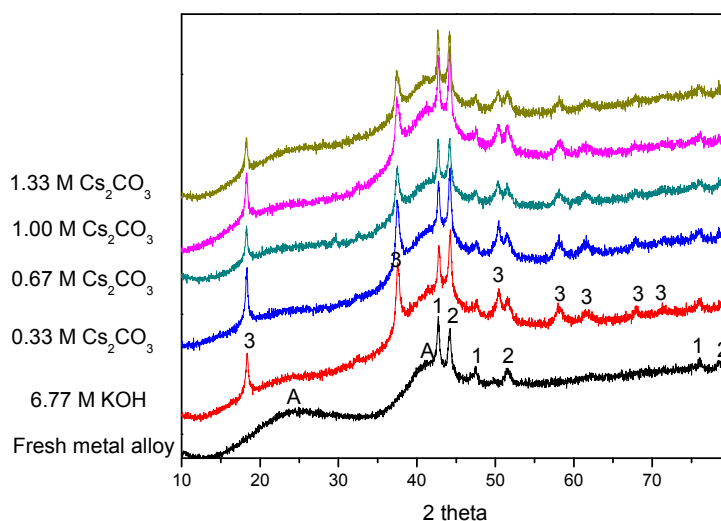

Figure 5. X-ray diffraction (XRD) patterns of the pristine and cycled AR3 in the 6.77 M KOH, 6.44 M KOH + 0.33 M Cs_2CO_3, 6.11 M KOH + 0.66 M Cs_2CO_3, 5.77 M KOH + 1.00 M Cs_2CO_3, and 5.44 M KOH + 1.33 M Cs_2CO_3 electrolytes. Note: Peaks marked as "A" represent the microcrystalline/amorphous components of $MgNi_2$ and Mg_2Ni; peaks marked as "1" and "2" represent metallic Mn and Co, respectively, and peaks marked as "3" represent $Mg(OH)_2$.

Table 4. Crystallite sizes in nm of the Mg_2Ni, $MgNi_2$, Co, Mn, and $Mg(OH)_2$ phases obtained from the XRD patterns in Figure 5.

Condition	Mg_2Ni	$MgNi_2$	Co	Mn	$Mg(OH)_2$
Pristine	0.5	0.6	28	41	-
Cycled in 6.77 M KOH	0.4	0.4	36	41	28
Cycled in 6.44 M KOH + 0.33 M Cs_2CO_3	0.5	0.6	34	62	28
Cycled in 6.11 M KOH + 0.66 M Cs_2CO_3	0.5	0.5	50	42	30
Cycled in 5.77 M KOH + 1.00 M Cs_2CO_3	0.6	0.5	34	40	22
Cycled in 5.44 M KOH + 1.33 M Cs_2CO_3	0.5	0.5	24	41	26

Table 5. Abundances in wt % of the Mg_2Ni, $MgNi_2$, Co, Mn, and $Mg(OH)_2$ phases, and the ratio between Mg_2Ni and $MgNi_2$ obtained from the XRD patterns in Figure 5.

Condition	Mg_2Ni	$MgNi_2$	Co	Mn	$Mg(OH)_2$	$Mg_2Ni/MgNi_2$
Pristine	53.5	35.7	6.5	4.3	-	1.50
Cycled in 6.77 M KOH	29.4	44.0	4.0	3.0	19.6	0.67
Cycled in 6.44 M KOH + 0.33 M Cs_2CO_3	39.2	32.1	4.3	2.6	21.8	1.22
Cycled in 6.11 M KOH + 0.66 M Cs_2CO_3	41.2	32.3	3.7	5.8	17.0	1.27
Cycled in 5.77 M KOH + 1.00 M Cs_2CO_3	42.8	35.1	6.7	4.9	10.5	1.22
Cycled in 5.44 M KOH + 1.33 M Cs_2CO_3	45.3	32.8	7.1	3.6	11.2	1.38

The chemical compositions of fresh and cycled MH alloys determined by ICP are compared in Table 6. Similar to the results in previous reports, the bulk composition changes slightly after cycling [5,6]. The loss of Mg occurs at approximately 1.5%, and results in an increase in the concentrations of other elements.

Table 6. ICP results in at % of the fresh and cycled AR3 in five different electrolytes.

Condition	Co	Ni	Mn	Mg
Pristine	2.94	38.17	5.69	53.20
Cycled in 6.77 M KOH	3.15	37.89	5.86	50.92
Cycled in 6.44 M KOH + 0.33 M Cs_2CO_3	3.10	39.16	5.59	52.25
Cycled in 6.00 M KOH + 0.77 M Cs_2CO_3	3.04	39.41	5.88	51.67
Cycled in 5.77 M KOH + 1.00 M Cs_2CO_3	3.04	39.56	6.19	51.21
Cycled in 5.44 M KOH + 1.33 M Cs_2CO_3	2.99	41.04	6.18	49.79

Cole–Cole plots obtained from the alternating current (AC) impedance measurements are shown in Figure 6. The reported equivalent circuit model for Ni-MH batteries using Mg-based alloy anodes is shown in Figure 7 [63–67]. Constant phase elements are used in this circuit model, due to the inhomogeneity properties of the electrode surface, such as porosity and roughness. Results obtained from the Cole–Cole plots are presented in Table 7. R_0 represents the resistance of ions traveling through the electrolyte and separator. The electrolyte containing 6.44 M KOH + 0.33 M Cs_2CO_3 shows the lowest R_0, which is consistent with its high discharge capacity, low degradation, and similar HRD compared with the 6.77 M KOH electrolyte. R_1 is the resistance among alloy particles and increases as the Cs_2CO_3 concentration increases. R_2 is the whole electrode resistance, and the addition of Cs_2CO_3 greatly decreases R_2 compared with the pure KOH electrolyte. C_1 represents the particle capacitance, which is closely related to the contact area among alloy particles. With increasing Cs_2CO_3 concentration, C_1 decreases. C_2 is the electrode capacitance, which is an indication of the amount of the active area in the electrode. Table 7 shows that the addition of Cs_2CO_3 decreases C_2 as well. The product of R_2 and C_2 represents the electrode activity performance [68,69], and a smaller value suggests better electrochemical performances. Table 7 shows an optimized $R_2 \cdot C_2$ value at 5.77 M KOH + 1.00 M Cs_2CO_3.
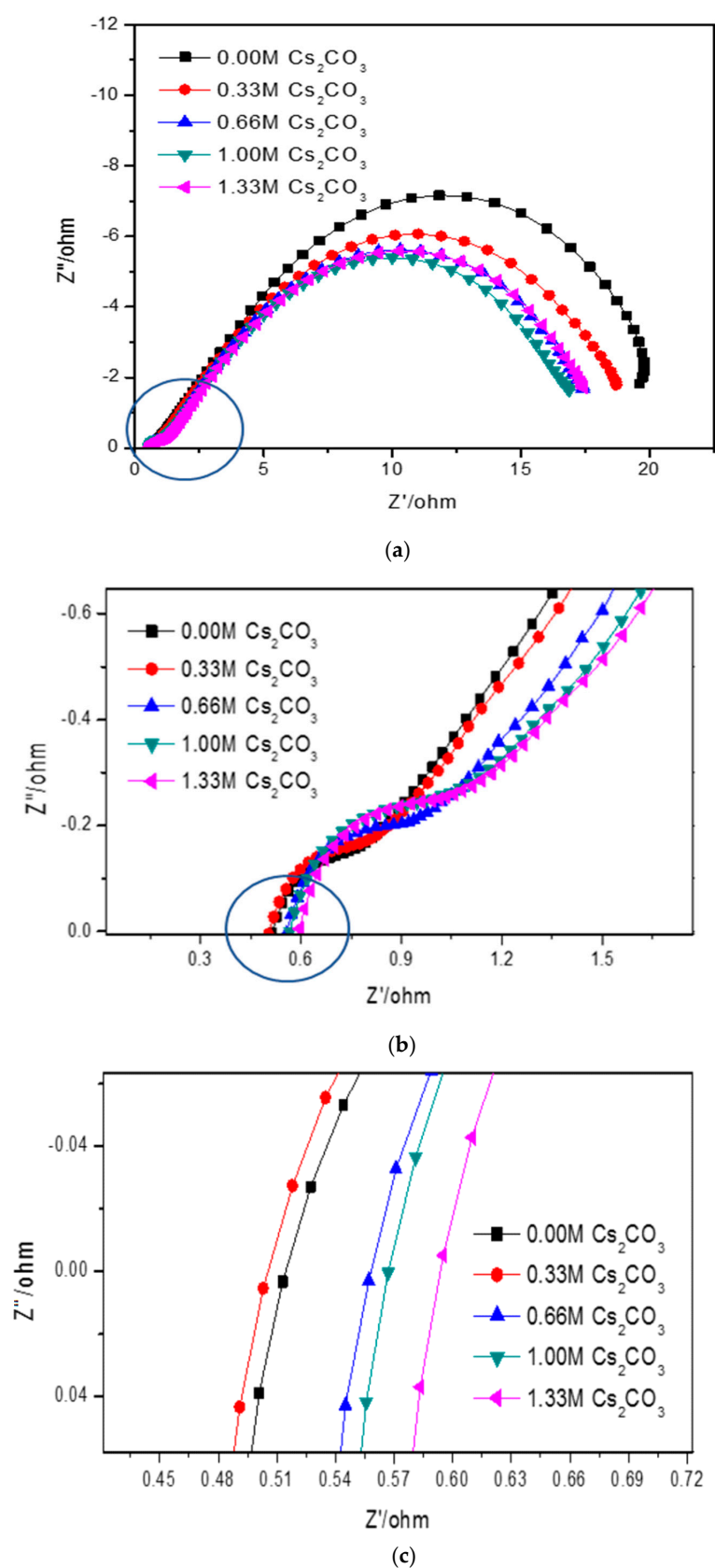
(a)

(b)

(c)

Figure 6. (**a**) Full Cole–Cole plots of AR3 in the 6.77 M KOH, 6.44 M KOH + 0.33 M Cs$_2$CO$_3$, 6.11 M KOH + 0.66 M Cs$_2$CO$_3$, 5.77 M KOH + 1.00 M Cs$_2$CO$_3$, and 5.44 M KOH + 1.33 M Cs$_2$CO$_3$ electrolytes, (**b**) magnification of the circled section in (**a**), and (**c**) magnification of the circled section in (**b**).
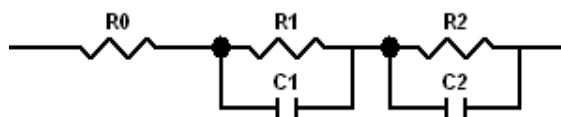
Figure 7. Proposed equivalent circuit model for NiMH batteries using Mg-based anodes [63].

Table 7. Data obtained by the AC impedance measurements of AR3 cycled in five different electrolytes.

Electrolyte Composition	R_0 (Ω·g)	R_1 (Ω·g)	C_1 (F·g^{-1})	R_2 (Ω·g)	C_2 (F·g^{-1})	$R_1·C_1$ (s)	$R_2·C_2$ (s)
6.77 M KOH	0.0369	0.0326	0.0033	1.2483	0.5929	1.079×10^{-4}	0.7401
6.44 M KOH + 0.33 M Cs$_2$CO$_3$	0.0363	0.0353	0.0022	1.1811	0.5786	7.812×10^{-5}	0.6834
6.00 M KOH + 0.77 M Cs$_2$CO$_3$	0.0400	0.0372	0.0019	1.0730	0.5357	7.115×10^{-5}	0.5748
5.77 M KOH + 1.00 M Cs$_2$CO$_3$	0.0407	0.0423	0.0018	1.0269	0.4629	7.490×10^{-5}	0.4753
5.44 M KOH + 1.33 M Cs$_2$CO$_3$	0.0417	0.0428	0.0017	1.0713	0.4643	7.099×10^{-5}	0.4974

3.3. Discussion

Results obtained from the current study indicate that the addition of Cs$_2$CO$_3$ alters the chemical and physical properties of the KOH electrolyte. As shown in Figure 6 and Table 7, an addition of 0.33 M Cs$_2$CO$_3$ decreases the solution resistance. Even if the electrolyte concentration was fixed at 6.77 M, the number of conductive ions increased with the addition of Cs$_2$CO$_3$. Therefore, the 6.44 M KOH + 0.33 M Cs$_2$CO$_3$ electrolyte has a decreased resistance and increased conductivity. While a low Cs$_2$CO$_3$ concentration promotes proton transfer in the system and improves both the discharge capacity and cycling performance, a higher Cs$_2$CO$_3$ concentration increases the solution resistivity due to the increased concentrations of larger cations (Cs$^+$) and anions (CO$_3{}^{2-}$) in the electrolyte, according to Stokes' Law [12].

Cs$_2$CO$_3$ also changes the alloy surface structure during cycling. The FTIR results show that a small addition of Cs$_2$CO$_3$ decreases the strength of surface metal–O bond, but generates the C–O bond on the alloy surface. By further increasing the Cs$_2$CO$_3$ concentration, the C=O bond begins to appear, in relation with decreasing C–O bond. The changes in surface groups by electrolyte additive consequently change the chemical and physical properties of the alloy particles. In our previous work [52], 32 types of salt additives in KOH electrolytes were tested, and some oxyacid salts were reported to create more surface groups that promoted proton transfer. In the current study, the addition of Cs$_2$CO$_3$ provides C–O and C=O bonds as new active sites for proton transfer. However, protons bond to the two active sites differently; protons are covalently bound to C–O, but electrostatically bound to C=O [52,66]. With the stronger attraction to C–O, more protons can be bound and later transferred (driven by voltage). Therefore, the largest number of C–O bonds, which occur at a small addition of Cs$_2$CO$_3$ (6.44 M KOH + 0.33 M Cs$_2$CO$_3$), were demonstrated to be the most effective in improving the electrochemical performances among all of the electrolytes tested in the current study.

The addition of Cs$_2$CO$_3$ also changes the bulk structure of the alloy particles. The TEM images show a layer of solid covering the MH alloy particle (Figure 3), which ranges from 20 nm to 500 nm. This surface layer decreases the contact area among alloy particles (as shown by the decrease in C_1) and increases the barrier for proton transfer among the particles (as shown by the increase in R_1). The ICP results show that a small amount of Cs$_2$CO$_3$ results in this decrease, but further increases in Cs$_2$CO$_3$ concentration increase the loss of Mg after cycling. For the pure KOH electrolyte, the alloy particles are covered by Mg(OH)$_2$. However, a small addition of Cs$_2$CO$_3$ reduces the particle size of Mg(OH)$_2$ on the surface, as indicated by the increase in full width at half maximum of the Mg(OH)$_2$ peaks (Figure 5). Smaller Mg(OH)$_2$ crystals are more strongly adsorbed on the surface of the MH alloy, which is not easily removed from the electrolyte, and also protects the bulk alloy from further oxidation. As the Cs$_2$CO$_3$ concentration further increases in the electrolyte, more MgCO$_3$ starts to form on the alloy surface. Since the solubility of MgCO$_3$ in KOH solution is greater than that of Mg(OH)$_2$, the loss of Mg occurs at a higher rate at higher Cs$_2$CO$_3$ concentrations. Therefore, high Cs$_2$CO$_3$ concentrations are not suggested for Mg–Ni alloys. On the other hand, if properly balanced with the loss of Mg,

an appropriate amount of carbonate formation by adding Cs_2CO_3 can promote the dissolution of surface oxidation products and consequently reveal a clean metal surface exposed to the electrolyte, which can lead to a decrease in electrode resistance (as shown by the decrease in R_2 as the Cs_2CO_3 concentration increases).

4. Conclusions

The effects of Cs_2CO_3 addition in a KOH-based electrolyte for Ni/MH batteries were investigated. Four different MH alloys (three Laves phase-related BCC and one MgNi-based) were used as the anode materials, and β-Ni(OH)$_2$ was used as the cathode material. A proper amount of Cs_2CO_3 addition greatly improved electrochemical performances. For the Laves phase-related BCC alloys, adding Cs_2CO_3 into the electrolyte improved the cycle stability (for all three alloys tested) and the discharge capacity (for Al-containing alloys). For the MgNi-based alloy, the discharge capacity increased to 132%, while degradation decreased to 87% in the 6.44 M KOH + 0.33 M Cs_2CO_3 electrolyte (compared with those in the 6.77 M KOH electrolyte). The effects of Cs_2CO_3 addition on the electrolyte and alloy properties are summarized as follows:

(1)   A small addition of Cs_2CO_3 decreases the electrolyte resistance and increases the conductivity.
(2)   A newly-formed fluffy C-containing surface oxide by the addition of Cs_2CO_3 is believed to be the main cause of the decrease in capacity decay during cycling.
(3)   The addition of Cs_2CO_3 in the electrolyte changes the alloy surface structure after cycling by creating more surface groups in addition to metal–O bonds, including C–O and C=O bonds, and the C–O bond is more effective than the C=O bond during proton transfer.
(4)   For MgNi-based alloys, the addition of Cs_2CO_3 changes the alloy bulk structure after cycling. A small addition of Cs_2CO_3 strengthens the Mg(OH)$_2$ layer on the alloy surface and prevents loss of Mg. However, a large addition of Cs_2CO_3 causes the formation of $MgCO_3$ with higher solubility in the KOH solution, and consequently a more severe loss of Mg.

Author Contributions: Shuli Yan designed and Peifeng Li performed the experiments, and analyzed the results. Jean Nei, Kwo-Hsiung Young, and Simon Ng provided guidance and helped in manuscript preparation.

Conflicts of Interest: The authors declare no conflict of interest.

Abbreviations

Ni/MH	Nickel/metal hydride
M	Metal
MH	Metal hydride alloy
MH	Hydrided metal
HRD	High-rate dischargeability
BCC	Body-centered-cubic
Cap_{high}	The highest value of discharge capacity in the initial 10 cycles
Cap_{low}	The lowest value of discharge capacity in the initial 10 cycles
n_{high}	The cycle number of the highest discharge capacity in the initial 10 cycles
n_{low}	The cycle number of the lowest discharge capacity in the initial 10 cycles
$n_{0,high}$	The cycle number of the highest discharge capacity in the initial 10 cycles for 6.77 M KOH electrolyte
$n_{0,low}$	The cycle number of the lowest discharge capacity in the initial 10 cycles for 6.77 M KOH electrolyte
FTIR	Fourier transform infrared
XRD	X-ray diffraction
TEM	Transmission electron microscopy

ICP-OES	Inductively coupled plasma-optical emission spectroscopy
AC	Alternating current
R_0	Resistance of ions traveling through the electrolyte and separator
R_1	Resistance among alloy particles
R_2	Whole electrode resistance
C_1	Particle capacitance
C_2	Electrode capacitance

References

1. Linden, D.; Reddy, T.B. *Handbook of Batteries*; McGraw-Hill: New York, NY, USA, 2002.

2. Fetcenko, M.A.; Ovshinsky, S.R.; Reichman, B.; Young, K.; Fierro, C.; Koch, J.; Zallen, A.; Mays, W.; Ouchi, T. Recent advances in NiMH battery technology. *J. Power Sources* **2007**, *165*, 544–551. [CrossRef]

3. Young, K.; Cai, X.; Chang, S. Reviews on the Chinese Patents regarding nickel/metal hydride battery. *Batteries* **2017**, *3*, 24. [CrossRef]

4. Young, K.; Ng, K.Y.S.; Bendersky, L.A. A Technical report of the robust affordable next generation energy storage system-BASF program. *Batteries* **2016**, *2*, 2. [CrossRef]

5. Chang, S.; Young, K.-H.; Nei, J.; Fierro, C. Reviews on the US Patents regarding nickel/metal hydride batteries. *Batteries* **2016**, *2*, 10. [CrossRef]

6. Ouchi, T.; Young, K.-H.; Moghe, D. Reviews on the Japanese Patent Applications regarding nickel/metal hydride batteries. *Batteries* **2016**, *2*, 21. [CrossRef]

7. Züttle, A. Materials for Hydrogen Storage. *Mater. Today* **2003**, 24–33. [CrossRef]

8. Zhao, X.; Ma, L. Recent progress in hydrogen storage alloys for nickel/metal hydride secondary batteries. *Int. J. Hydrog. Energy* **2009**, *34*, 4788–4796. [CrossRef]

9. Ouyang, L.; Huang, J.; Wang, H.; Liu, J.; Zhu, M. Progress of hydrogen storage alloys for Ni-MH rechargeable power batteries in electric vehicles: A review. *Mater. Chem. Phys.* **2017**, *200*, 164–178. [CrossRef]

10. Yu, X.B.; Wu, Z.; Xia, B.J.; Xu, N.X. A Ti-V-Based BCC phase alloy for use as metal hydride electrode with high discharge capacity. *J. Chem. Phys.* **2004**, *121*, 987–990. [CrossRef] [PubMed]

11. Young, K.; Nei, J. The current status of hydrogen storage alloy development for electrochemical applications. *Materials* **2013**, *6*, 4574–4608. [CrossRef] [PubMed]

12. Nei, J.; Young, K.; Rotarov, D. Studies on MgNi-based metal hydride electrode with aqueous electrolytes composed of various hytproxides. *Batteries* **2016**, *2*, 27. [CrossRef]

13. Redzeb, M.; Zlatanova, Z.; Spassov, T. Influence of boron on the hydriding of nanocrystalline Mg_2Ni. *Intermetallics* **2013**, *34*, 63–68. [CrossRef]

14. Nikkuni, F.R.; Santos, S.F.; Ticianelli, E.A. Microstructures and electrochemical properties of $Mg_{49}Ti_6Ni_{45-x}M_x$ (M = Pd and Pt) alloy electrodes. *Int. J. Energy Res.* **2013**, *37*, 706–712. [CrossRef]

15. Zhang, X.; Belharouak, I.; Li, L.; Lei, Y.; Elam, J.W.; Nie, A.; Chen, X.; Yassar, R.S.; Axelbaum, R.L. Structural and electrochemical study of Al_2O_3 and TiO_2 coated $Li_{1.2}Ni_{0.13}Mn_{0.54}Co_{0.13}O_2$ cathode material using ALD. *Adv. Energy Mater.* **2013**, *3*, 1299–1307. [CrossRef]

16. Zhang, Y.; Li, C.; Cai, Y.; Hu, F.; Liu, Z.; Guo, S. Highly improved electrochemical hydrogen storage performances of the Nd-Cu-added Mg_2Ni-type alloys by melt spinning. *J. Alloy. Compd.* **2014**, *584*, 81–86. [CrossRef]

17. Wang, Y.T.; Wan, C.B.; Wang, R.L.; Meng, X.H.; Huang, M.F.; Ju, X. Effect of Cr substitution by Ni on the cycling stability of Mg_2Ni alloy using EXAFS. *Int. J. Hydrog. Energy* **2014**, *39*, 14858–14867. [CrossRef]

18. Hou, X.; Hu, R.; Zhang, T.; Kou, H.; Song, W.; Li, J. Microstructure and electrochemical hydrogenation/dehydrogenation performance of melt-spun La-doped Mg_2Ni alloys. *Mater. Charact.* **2015**, *106*, 163–174. [CrossRef]

19. Verbovytskyy, Y.; Zhang, J.; Cuevas, F.; Paul-Boncour, V.; Zavaliy, I. Synthesis and properties of the $Mg_2Ni_{0.5}Co_{0.5}H_{4.4}$ hydride. *J. Alloy. Compd.* **2015**, *645*, S408–S411. [CrossRef]

20. Li, M.; Zhu, Y.; Yang, C.; Zhang, J.; Chen, W.; Li, L. Enhanced electrochemical hydrogen storage properties of Mg_2NiH_4 by coating with nano-nickel. *Int. J. Hydrog. Energy* **2015**, *40*, 13949–13956. [CrossRef]

21. Shang, J.; Ouyang, Z.; Liu, K.; Xing, C.; Liu, W.; Wang, L. Effect of Li atom infiltration by the way of electro-osmosis on electrochemical properties of amorphous $Mg_{65}Ni_{27}La_8$ alloy used as negative electrode materials for the nickel–metal hydride secondary batteries. *J. Non-Cryst. Solids* **2015**, *415*, 30–35. [CrossRef]

22. Shao, H.; Li, X. Effect of nanostructure and partial substitution on gas absorption and electrochemical properties in Mg_2Ni-based alloys. *J. Alloy. Compd.* **2016**, *667*, 191–197. [CrossRef]

23. Ohara, R.; Lan, C.-H.; Hwang, C.-S. Electrochemical and structural characterization of electroless nickel coating on Mg_2Ni hydrogen storage alloy. *J. Alloy. Compd.* **2013**, *580*, S368–S372. [CrossRef]

24. Shahcheraghi, A.; Dehghani, F.; Raeissi, K.; Saatchi, A.; Enayati, M.H. Effects of TiO_2 additive on electrochemical hydrogen storage properties of nanocrystalline/amorphous Mg_2Ni intermetallic alloy. *Iran. J. Mater. Sci. Eng.* **2013**, *10*, 1–9.

25. Haghighat-Shishavan, S.; Bozorg, F.K. Nano-crystalline $Mg_{2-x}Mn_xNi$ compounds synthesized by mechanical alloying: Microstructure and electrochemistry. *J. Ultrafine Grained Nanostruct. Mater.* **2014**, *47*, 43–49.

26. Venkateswari, A.; Nithya, C.; Kumaran, S. Electrochemical behaviour of $Mg_{67}Ni_{33-x}Nb_x$ (x = 0, 1, 2 and 4) alloy synthesized by high energy ball milling. *Proc. Mater. Sci.* **2014**, *5*, 679–687. [CrossRef]

27. Rubin, E.J.; Baboian, R. A correlation of the solution properties and the electrochemical behavior of the nickel hydroxide electrode in binary aqueous alkali hydroxides. *J. Electrochem. Soc.* **1971**, *118*, 428–433. [CrossRef]

28. Barnard, R.; Randell, C.F.; Tye, F.L. Studies concerning changes nickel hydroxide electrodes. IV. Reversible potentials in LiOH, NaOH, RbOH and CdOH. *J. Appl. Electrochem.* **1981**, *11*, 517–523. [CrossRef]

29. Oliva, P.; Leonardi, J.; Laurent, J.F.; Delmas, C.; Braconnier, J.J.; Figlarz, M.; Fievet, F.; Guibert, A. Review of the structure and the electrochemistry of nickel hydroxides and oxy-hydroxides. *J. Power Sources* **1982**, *8*, 229–255. [CrossRef]

30. Leblanc, P.; Jordy, C.; Knosp, B.; Blanchard, Ph. Mechanism of alloy corrosion and consequences on sealed nickel-metal hydride battery performance. *J. Electrochem. Soc.* **1998**, *145*, 860–863. [CrossRef]

31. Knosp, B.; Vallet, L.; Blamchard, P. Performance of an AB_2 alloy in sealed Ni-MH batteries for electric vehicles: Qualification of corrosion rate and consequences on the battery performance. *J. Alloy. Compd.* **1999**, *293–295*, 770–774. [CrossRef]

32. Jeong, Y.H.; Kim, H.G.; Jung, Y.H.; Ruhmann, H. Effect of LiOH, NaOH and KOH on Corrosion and Oxide Microstructure of Zr-Based Alloys. Available online: http://www.iaea.org/inis/collection/NCLCollectionStore/_Public/30/060/30060383.pdf (accessed on 26 February 2016).

33. Liu, J.; Wang, D.; Liu, S.; Feng, X. Improving high temperature performance of MH/Ni battery by orthogonal design. *Battery Bimon.* **2003**, *33*, 218–220.

34. Hou, X.; Nan, J.; Han, D.; Zhao, J. Preparation and performance of high-rated A-type MN-Ni batteries. *Chin. J. Appl. Chem.* **2004**, *21*, 1169–1173.

35. Lv, J.; Liu, X.; Zhang, J.; Fan, L.; Wang, L.; Zhang, Z. Studies on high-power nickel-metal hydride battery. *Chin. J. Power Sources* **2005**, *29*, 826–830.

36. Li, X.; Dong, H.; Zhang, A.; Wei, Y. Electrochemical impedance and cyclic voltammetry characterization of a metal hydride electrode in alkaline electrolytes. *J. Alloy. Compd.* **2006**, *426*, 93–96. [CrossRef]

37. Park, C.; Shim, J.; Jang, M.; Park, C.; Choi, J. Influences of various electrolytes on the low-temperature characteristics of Ni-MH secondary battery. *Trans. Korean Hydrog. New Energy Soc.* **2007**, *18*, 284–291.

38. Chen, R.; Li, L.; Wu, F.; Qiu, X.; Chen, S. Effects of low temperature on performance of hydrogen-storage alloys and electrolyte. *Min. Metall. Eng.* **2007**, *27*, 44–46.

39. Yang, D.C.; Park, C.N.; Park, C.J.; Choi, J.; Sim, J.S.; Jang, M.H. Design of additives and electrolyte for optimization of electrode characteristics of Ni-MH secondary battery at room and low temperatures. *Trans. Korean Hydrog. New Energy Soc.* **2007**, *18*, 365–373.

40. Zhang, X.; Chen, Y.; Tao, M.; Wu, C. Effect of electrolyte concentration on low-temperature electrochemical properties of $LaNi_5$ alloy electrode at 233 K. *J. Rare Earths* **2008**, *26*, 402–405. [CrossRef]

41. Zhang, X.; Chen, Y.; Tao, M.; Wu, C. Effect of electrolyte on the low-temperature electrochemical properties of $LaNi_5$ alloy electrode at 253 K. *Rare Metal Mater. Eng.* **2008**, *37*, 2012–2015.

42. Pei, L.; Yi, S.; He, Y.; Chen, Q. Effect of electrolyte formula on the self-discharge properties of nickel-metal hydride batteries. *J. Guangdong Univ. Technol.* **2008**, *25*, 10–12.

43. Khaldi, C.; Mathlouthi, H.; Lamloumi, J. A comparative study of 1 M and 8 M KOH electrolyte concentrations used in Ni-MH batteries. *J. Alloy. Compd.* **2009**, *469*, 464–471. [CrossRef]

44. Guiose, B.; Cuevas, F.; Décamps, B.; Leroy, E.; Percheron-Guégan, A. Microstructural analysis of the aging of pseudo-binary (Ti, Zr)Ni intermetallic compounds as negative electrodes of Ni-MH batteries. *Electrochim. Acta* **2009**, *54*, 2781–2789. [CrossRef]

45. Qiu, Z.; Wu, A. Study on wide temperature characteristics of Ni-MH battery. *J. South China Norm. Univ.* **2009**, *1*, 79–81.

46. Song, M.; Chen, Y.; Tao, M.; Wu, C.; Zhu, D.; Yang, H. Some factors affecting the electrochemical performances of LaCrO$_3$ as negative electrodes for Ni/MH batteries. *Electrochim. Acta* **2010**, *55*, 3103–3108. [CrossRef]

47. Ma, H.; Cheng, F.; Chen, J. Nickel-metal hydride (Ni-MH) rechargeable battery. In *Electrochemical Technologies for Energy Storage and Conversion*; Zhang, J., Zhang, L., Liu, H., Sun, A., Liu, R., Eds.; John Wiley & Sons, Inc.: New York, NY, USA, 2011; p. 204.

48. Karwowska, M.; Jaron, T.; Fijalkowski, K.J.; Leszczynski, P.J.; Rogulski, Z.; Czerwinski, A. Influence of electrolyte composition and temperature on behavior of AB$_5$ hydrogen storage alloy used as negative electrode in Ni-MH batteries. *J. Power Sources* **2014**, *263*, 304–309. [CrossRef]

49. Giza, K. Influence of electrolyte on capacity and corrosion resistance of anode material used in Ni-MH cells. *Ochr. Przed Koroz.* **2016**, *59*, 167–169. [CrossRef]

50. Shangguan, E.; Li, J.; Chang, Z.; Tang, H.; Li, B.; Yuan, X.; Wang, H. Sodium tungstate as electrolyte additive to improve high-temperature performance of nickelemetal hydride batteries. *Int. J. Hydrog. Energy* **2013**, *38*, 5133–5138. [CrossRef]

51. Vaidyanathan, H.; Robbins, K.; Rao, G.M. Effect of KOH concentration and anions on the performance of an Ni-H$_2$ battery positive plate. *J. Power Sources* **1996**, *63*, 7–13. [CrossRef]

52. Yan, S.; Ng, K.Y.S.; Young, K.-H. Effects of salt additives to the KOH electrolyte used in Ni/MH batteries. *Batteries* **2015**, *1*, 54–73. [CrossRef]

53. Li, L. Non-Toxic Alkaline Electrolyte with Additives for Rechareable Zinc Cells. U.S. Patent 2010/0062327, 11 March 2010.

54. Young, K.; Nei, J.; Wong, D.; Wang, L. Structural, hydrogen storage, and electrochemical properties of Laves-phase related body-centered-cubic solid solution metal hydride alloys. *Int. J. Hydrog. Energy* **2014**, *39*, 21489–21499. [CrossRef]

55. Young, K.; Ouchi, T.; Nei, J.; Wang, L. Annealing effects on Laves phase-related body-centered-cubic solid solution metal hydride alloys. *J. Alloy. Compd.* **2016**, *654*, 216–225. [CrossRef]

56. Ruiz, F.C.; Martínez, P.S.; Castro, E.B.; Humana, R.; Peretti, H.A.; Visintin, A. Effect of electrolyte concentration on the electrochemical properties of an AB$_5$-type alloy for Ni/MH batteries. *Int. J. Hydrog. Energy* **2013**, *38*, 240–245. [CrossRef]

57. Martínez, P.S.; Ruiz, F.C.; Visintin, A. Influence of different electrolyte concentrations on the performance of an AB$_2$-type alloy. *J. Electrochem. Soc.* **2014**, *161*, A326–A329. [CrossRef]

58. Yasuoka, S.; Magari, Y.; Murata, T.; Tanaka, T.; Ishida, J.; Nakamura, H.; Nohma, T.; Kihara, M.; Baba, Y.; Teraoka, H. Development of high-capacity nickel-metal hydride batteries using superlattice hydrogen-absorbing alloys. *J. Power Sources* **2006**, *156*, 662–666. [CrossRef]

59. Why is Aluminum Carbonate Unstable? Available online: https://chemistry.stackexchange.com/questions/6369/why-is-aluminium-carbonate-unstable (accessed on 16 August 2017).

60. Yang, C.; Wöll, C. IR spectroscopy applied to metal oxide surfaces: Adsorbate vibrations and beyond. *Adv. Phys.* **2017**, *2*, 373–408. [CrossRef]

61. Reig, F.B.; Adelantado, J.V.; Moya Moreno, M.C. FTIR quantitative analysis of calcium carbonate (calcite) and silica (quartz) mixtures using the constant ratio method. Application to geological samples. *Talanta* **2002**, *58*, 811–821. [CrossRef]

62. Young, K. Stoichiometry in inter-metallic compounds for hydrogen storage applications. In *Stoichiometry and Materials Science—When Numbers Matter*; Innocenti, A., Kamarulzaman, N., Eds.; InTech: Rijeka, Crotia, 2012.

63. Zhang, W.; Kumar, M.P.S.; Srinivasan, S. AC impedance studies on metal hydride electrodes. *J. Electrochem. Soc.* **1995**, *142*, 2935–2943. [CrossRef]

64. Chang, S.; Young, K.; Ouchi, T.; Meng, T.; Nei, J.; Wu, X. Studies on incorporation of Mg in Zr-based AB$_2$ metal hydride alloys. *Batteries* **2016**, *2*, 11. [CrossRef]

65. Trapanese, M.; Franzitta, V.; Viola, A. Description of hysteresis of nickel metal hydride battery. In Proceedings of the 38th Annual Conference on IEEE Industrial Electronics Society, Montreal, QC, Canada, 25–28 October 2012; pp. 967–970.

66.　Trapanese, M.; Franzitta, V.; Viola, A. Description of hysteresis in lithium battery by classical Preisach model. *Adv. Mater. Res.* **2013**, *622*, 1099–1103.

67.　Trapanese, M.; Franzitta, V.; Viola, A. The Jiles Atherton model for description on hysteresis in lithium battery. In Proceedings of the Twenty-Eighth Annual IEEE Applied Power Electronics Conference and Exposition (APEC), Long Beach, CA, USA, 17–21 March 2013; pp. 2772–2775.

68.　Young, K.; Ouchi, T.; Nei, J.; Moghe, D. The importance of rare-earth additions in Zr-based AB_2 metal hydride alloys. *Batteries* **2016**, *2*, 25. [CrossRef]

69.　Grabowski, J.S. What is the covalency of hydrogen bonding? *Chem. Rev.* **2011**, *111*, 2597–2625. [CrossRef] [PubMed]